Coherent diffractive imaging of solid state reactions in zinc oxide crystals

2011 New J. Phys. 13 113009

(http://iopscience.iop.org/1367-2630/13/11/113009)

New Journal of Physics
The open-access journal for physics

Coherent diffractive imaging of solid state reactions in zinc oxide crystals

Steven J Leake[1,4,5], **Ross Harder**[2] **and Ian K Robinson**[1,3]

[1] London Centre for Nanotechnology, University College London, Gower Street, WC1E 6BT, UK
[2] Argonne National Laboratory, 9700 South Cass Avenue, Argonne, IL 60439, USA
[3] Diamond Light Source, Harwell Campus, Didcot OX11 0DE, UK
E-mail: steven.leake@psi.ch

New Journal of Physics **13** (2011) 113009 (14pp)
Received 15 April 2011
Published 9 November 2011
Online at http://www.njp.org/
doi:10.1088/1367-2630/13/11/113009

Abstract. We investigated the doping of zinc oxide (ZnO) microcrystals with iron and nickel via *in situ* coherent x-ray diffractive imaging (CXDI) in vacuum. Evaporated thin metal films were deposited onto the ZnO microcrystals. A single crystal was selected and tracked through annealing cycles. A solid state reaction was observed in both iron and nickel experiments using CXDI. A combination of the shrink wrap and guided hybrid–input–output phasing methods were applied to retrieve the electron density. The resolution was 33 nm (half order) determined via the phase retrieval transfer function. The resulting images are nevertheless sensitive to sub-angstrom displacements. The exterior of the microcrystal was found to degrade dramatically. The annealing of ZnO microcrystals coated with metal thin films proved an unsuitable doping method. In addition the observed defect structure of one crystal was attributed to the presence of an array of defects and was found to change upon annealing.

[4] Present Address: Paul Scherrer Institut, CH-5232 Villigen PSI, Switzerland.
[5] Author to whom any correspondence should be addressed.

Contents

1. Introduction

An industrial nanomaterial for many decades, zinc oxide (ZnO) has seen wide application in the manufacture of paints, rubber products, pharmaceuticals and sun screen among others. Its versatility is defined by its tunable properties; a wide direct band gap II–VI semiconductor that exhibits both n-type conductivity and, when doped, p-type conductivity (group V elements). Dopant control allows the electrical properties to be varied from an insulator through an n-type semiconductor to a metal whilst maintaining optical transparency. Exhibiting both piezoelectric and pyroelectric nature, ZnO has also been identified, when doped, as a potential dilute magnetic semiconductor applicable in spintronics.

A recent review by Davies *et al* [7] regarding the doping of ZnO describes the present state of the field. Here we focus on the transition metals Fe and Ni due to recent observations of improved luminescence [1], conductivity [3, 30] and calculation suggesting room temperature ferromagnetism [8]. Based on the electronegativities of Fe and Ni being larger than Zn these elements should substitute at the Zn site upon annealing. A variety of methods have been used to date for fabrication including ion implantation, sol–gel, pulsed laser deposition and solid state methods. An array of conclusions have been drawn regarding the solubility of these transition elements into the ZnO lattice. Several thin film studies show dopant concentrations between 0–30 at.% [15, 18, 30, 32]. In both bulk and powder samples concentrations of Fe at 2–7 at.% [2, 31] were found between 500–800 °C beyond which secondary phases, Fe_2O_3 and Fe_3O_4, formed. To our knowledge, few studies exist of Ni integration into the ZnO lattice—in thin films, 3 at.% was observed by Mandal *et al* [18] and in bulk crystalline samples, Bates *et al* reported 1 at.% [2]. The addition of dopants will alter the lattice parameter of the material, thus a technique sensitive on this scale is required to elucidate their presence.

Coherent x-ray diffraction imaging (CXDI) is a rapidly advancing non-destructive technique with the potential to determine quantitative displacement fields present in crystalline materials [25, 26]. When a finite crystal is illuminated with a coherent x-ray beam, the diffracted intensity distribution observed in the vicinity of each Bragg peak is sensitive to subtle displacements in the crystal structure along the direct space (DS) scattering vector direction. If sampled sufficiently using iterative methods the phase of the complex amplitude lost during the measurement can be recovered, the DS electron density determined and the displacement fields present realized. The measurement of additional Bragg peaks allows one to deduce multi-dimensional components of the displacements and compute the strain tensor [24], however this is beyond the scope of this paper.

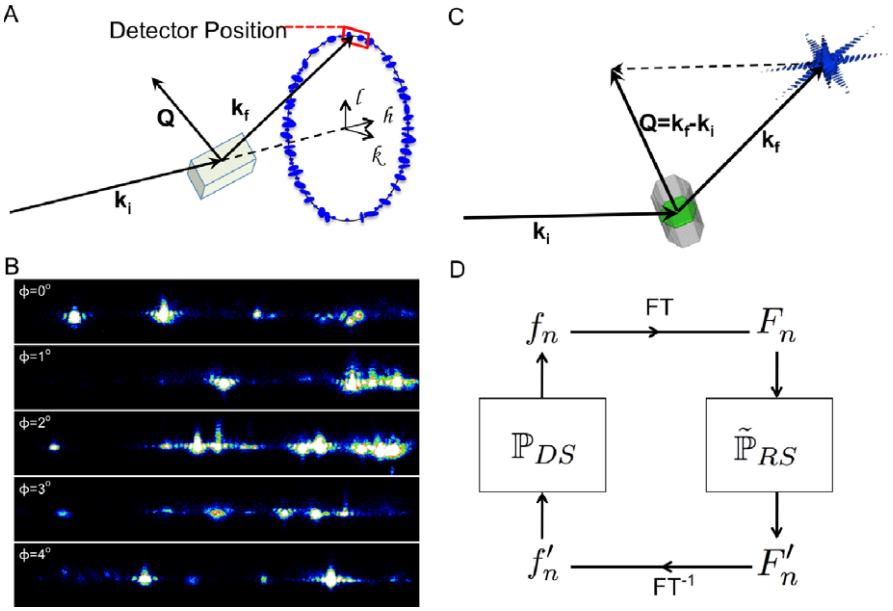

Figure 1. (A) Diffraction geometry, where the incident and diffracted wave vectors are denoted k_i and k_f respectively, from a sample covered with thousands of randomly oriented crystals a powder ring is observed. (B) Detector image at a fixed point in reciprocal space (RS) as a function of sample rotation, ϕ, about the Q-vector. Here crystals with similar orientations are brought into and out of diffraction. (C) A single isolated crystal illuminated with coherent x-rays, the diffraction geometry and the expected continuous intensity distribution surrounding the Bragg peak. (D) The iterative phase retrieval algorithm traverses DS and RS via Fourier transform (FT). Employing constraints in each space via the projection formalism, $\mathbb{P}$, where n is the iteration number a suitable estimate of the missing phases is achieved.

Here we investigate a single ZnO microrod using CXDI in vacuum during an *in situ* solid state reaction with an evaporated iron layer, similar experiments with nickel will also be discussed.

2. Methods

ZnO crystals were tailored in both morphology, size and aspect ratio using the chemical vapour transport deposition method detailed elsewhere [16]. High yields of the rod morphology, a hexagonal prism of wurtzite ZnO approximately $\sim$1 μm in diameter and with length to width ratio 3 : 2 were deposited on Si(111) substrates. The crystals were grown to these characteristics to obtain sufficient scattered intensity from an approximately fully coherent illumination [17]. The crystals were distributed across the substrate in random orientations. The SiO_2 layer was grown thermally to adhere the crystals to the substrates in order to maintain stability during the subsequent experiments. An unfocussed 8.9 keV x-ray beam at Advanced Photon Source beamline 34-ID-C was directed onto the sample. Akin to a traditional powder diffraction experiment a large beam footprint on the sample illuminates many crystals and those which satisfy the Bragg law result in a ring of incoherent diffracted intensity, see figure 1(A). Two

crystal orientations are preferable, stood on an end $\{001\}/\{00\bar{1}\}$ facet or laying on a side $\{100\}$ facet. Placing the charge-coupled device detector at a (002) Bragg reflection, see figure 1(B), a number of crystals oriented in the same direction are observed on the powder ring. Rotating the sample brings other crystals with slightly different orientations into and out of diffraction as the Bragg law is satisfied. Reducing the beam footprint allows a single crystal to be isolated and the continuous intensity distribution surrounding the Bragg peak sampled, see figure 1(C). The diffraction surrounding each Bragg peak describes the shape of the illuminated crystal and is sensitive to internal displacements along the Q-vector direction. When the intensity is measured, $I = |A|^2$, the phase information encoded in the interference pattern is lost. By sufficiently oversampling above the Nyquist rate[6] [20, 21, 27] of the intensity distribution, iterative algorithms are then used to employ *a priori* knowledge of the crystal in both DS and RS to find a set of phases consistent with the measured intensity data. Figure 1(D) shows the basic algorithm operation in terms of projection operators ($\mathbb{P}$) [9], where specific constraints are applied to the current best estimate f_n of the calculation in both DS and RS. The mathematical Fourier transform (FT) which describes the translation between DS and RS is calculated discretely using the fast Fourier transform (FFT).

It has been shown previously [17, 24] that a single ZnO crystal can be isolated and multiple Bragg reflections measured. In order to manipulate the crystals *in situ*, the samples were mounted in a vacuum chamber [16], 10^{-8} mbar. In this set up it was not possible to obtain the required precision to locate and orient a single crystal. Thus a sample with many thousands of crystals was illuminated. A single crystal was isolated by reducing the beam footprint on the sample, via the closing of slits. The chosen crystal was tracked through deposition of a metal layer and subsequent annealing steps. To preserve the crystals present state, annealing and cooling cycles were carried out with the sample always measured at a reference temperature, where the crystal was found to be stable after each cycle, this process is defined as an 'annealing step'. To obtain sufficient statistics for CXDI with low resolution a 3 hour scan was required after each annealing step. Several experiments determined the crystals to be in the same state after an evaporation of Fe and Ni, and was observed to be independent of deposited film thickness. The reference temperature of approximately 300°C was found to be suitable whereby no variation in diffraction was observed. However, close enough to the reaction temperature that the diffraction does not move completely out of the detector upon further annealing. Annealing proceeded for 5 and 10 minute periods up to 400 °C after which the sample was cooled and measured until a reaction was observed. By gradually altering the annealing step the onset of the solid state chemical reaction was sought, subsequent quenching to a reference temperature would prevent a continuation of the reaction while the measurement was made. This had three advantages; firstly, the crystal was not changing during measurement, secondly, the phasing parameters could be kept constant as thermal expansion effects could be neglected and thirdly, the Bragg spot proved highly reproducible. In the case of a large structural change the remaining crystal could be found and measured by returning to the logged motor positions for the previous measurement[7].

[6] The Nyquist rate is defined as twice the maximum frequency observed in the signal [21].

[7] Attempts were made to observe the crystal change during the annealing steps using 2D analysis (1000 accumulations, 50s total exposure). Any observable variation was difficult to identify by eye as there was no guarantee at each temperature the same 2D slice through the crystals Bragg spot was being sampled. Subsequent reconstructions proved too slow to have an impact on the decision to cool the sample and suffered from inconsistencies due to the miscentring of the diffraction peak [16].

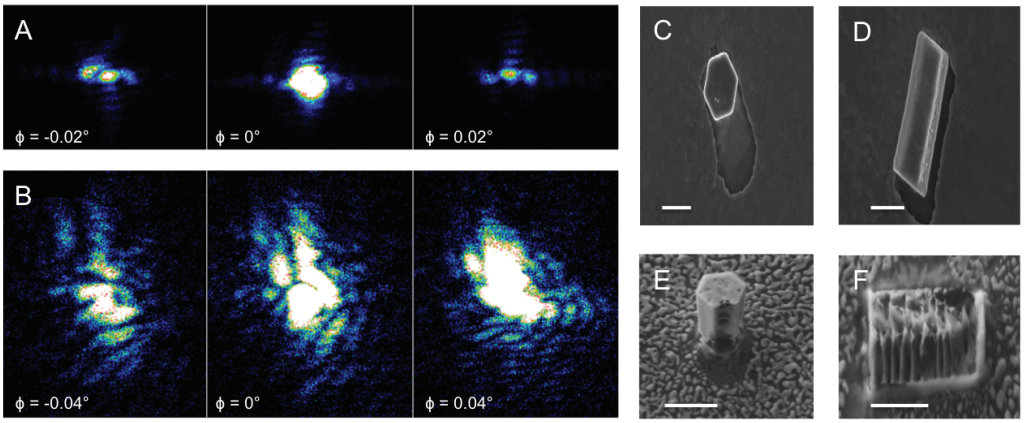

Figure 2. Diffraction patterns observed at different positions in the rocking curve, either side and through the Bragg peak for a ZnO crystal (A) at 298 °C after Fe deposition and (B) after further annealing up to 358 °C. SEM images, (C, D), of Fe coated ZnO crystals at different orientations to the substrate annealed to 450 °C, (E, F), annealed to 600 °C. Scale bar = 1 μm.

3. Observations

Initial observations of the Bragg peak of a ZnO nanorod post Fe deposition are shown in figures 2 (A) and (B). The stark contrast between diffraction from a heated crystal (A) tracked through annealing to a higher temperature (B) is clear. The crystal has decreased in size as the interference fringe separation has become larger. A dramatic increase in exposure time from 0.1 to 2 s was required to obtain the same level of statistics and the need for a wider rocking curve confirms a solid state chemical reaction between Fe and ZnO has taken place on a relatively large scale. The reaction proceeds at a relatively low temperature of 350 °C considering Bates *et al* [2] observed a solubility of zero at 500 °C increasing as a function of temperature to 7 at.% at 800 °C. A solubility of this order does not explain the large variation in diffraction. We would expect a severe degradation starting near the surface due to the formation of Fe dominated crystal structures upon diffusion leading to fractured ZnO crystals. In one case, a crystal began to move away from its previously adhered location, it was tracked for 1 h over 1° in angle. Its movement prevented a measurement. However, upon returning to its original location a remnant similar to that observed in figure 2(B) was observed suggesting part of the crystal detached or was distorted beyond the sensitivity of CXDI. It is important to note CXDI is sensitive to a specific crystal structure. The formation of aggregates with different crystal structures lead to diffraction elsewhere in RS hence we would expect to see the measured intensity drop as fewer scatterers contribute to our localized diffraction pattern.

The low temperature observed can be explained by heating of the nanocrystal due to the illuminating beam and the presence of large errors in the temperature measurement. Inspection of the silicon as it began to conduct suggested a good temperature calibration as the silicon substrate began to glow orange at 600 °C. However, the heating was asymmetric and large gradients were evident across the sample. The thermocouple was positioned on a mounting plate attached to a screw and measures a region of the sample approximately 5 mm from the illuminated sample region.

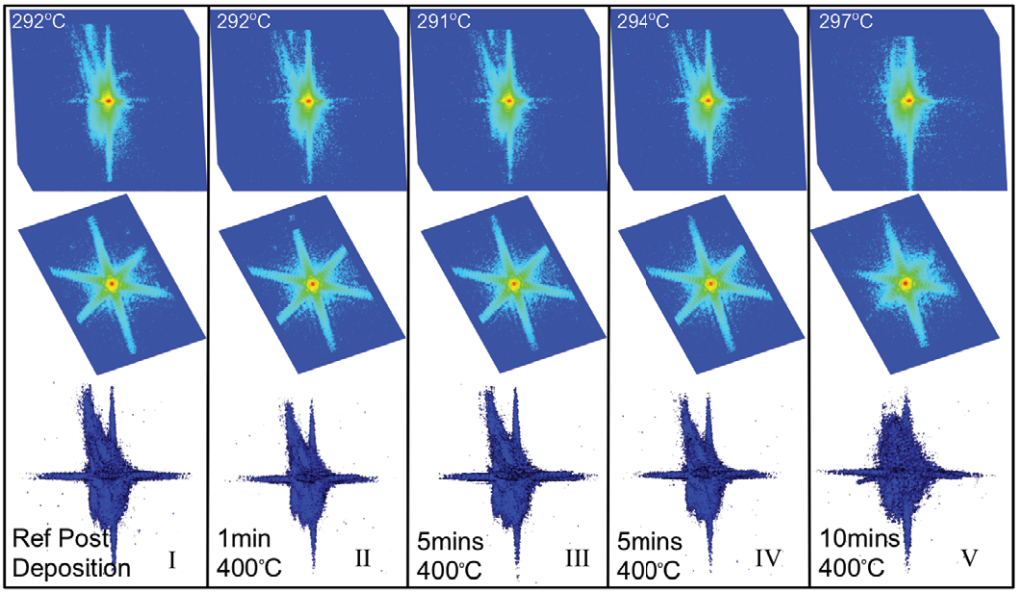

Figure 3. Two orthogonal log scale cut planes through the geometrically corrected measured intensities at the (101) Bragg peak and a 3D render for comparison of the same ZnO crystal with a 60nm deposited Fe layer annealed through four steps, II–V, after a reference measurement, I. The temperature of the crystal during each CXDI measurement is noted in the top left of each pane.

The structural change was later confirmed with scanning electron microscopy (SEM), see figures 2(C)–(F). A sample was annealed through to 358 °C and post experiment SEM analysis, shown in (C) and (D), confirms the presence of crystals coated with a layer of Fe but no obvious change in morphology. The shadow is due to the angle of evaporation and means only the top and three of the hexagonal facets are coated in metal. A second sample where similar diffraction changes were observed when the crystal was heated to 600 °C is shown in (E) and (F). At this temperature the layer of Fe has dewetted the surface and the internal degradation of the crystals observed. This confirms the large variation in the x-ray diffraction data and highlights the ability of CXDI to observe the initial stages of the reaction before the morphology of the crystals change. It also emphasizes the potential of CXDI for the investigation of buried structures.

The diffraction pattern in figure 2(B) could not be inverted because the reaction was ongoing during the measurement. In addition, the phase constraints imposed on (A) were invalid as the two measurements were carried out at different temperatures. This led to the development of the annealing step procedure described in section 2 to observe the onset of diffusion of the deposited species into the crystal. An example of a crystal covered in Fe, annealed through four steps (II–IV) after a reference measurement (I) is shown in figure 3. The 2D cut planes demonstrate the two fold and six-fold symmetries expected for a hexagonal prism morphology, the modulation in the diffraction arises from the interference between crystal truncation rods from the surfaces of parallel facets. Little change was observed in the first three annealing steps after deposition. The only discernible difference is the noise present in the measurement and we expected this to be reproduced in the reconstructions. The final annealing step shows a considerable change, although not as significant as seen previously because here the exposure

time and rocking curve remained constant for all scans. We can therefore expect to observe subtle variations in the displacement field within the crystal, of the order of a few lattice parameters across the entire crystal, as opposed to the large variations demonstrated in figure 2. It is also important to note the asymmetry present around the Bragg peak, as this provides evidence for the presence of displacement fields in the crystal. Thus, in this case, the crystal was in a strained state before further annealing, due to the presence of defect structures.

4. Results: phasing

The 'phase problem', the need to assign phases to the measured amplitudes to allow FT, is the main challenge of the data analysis. The phase problem is known to have multiple ambiguous solutions, which may be only partially excluded by the application of constraints. Two approaches exist to overcome these problems, firstly, ambiguous solution identification [4, 33] and secondly, averaging results from multiple random starting points to maintain distinct structural features [5, 6, 29]. A combination of the two will be implemented here as they are both advantageous for different reasons. The first makes the second applicable and averaging highlights reproducible phase features and suppresses erroneous phase features.

The phasing constraint with the largest impact on the reconstructed solution is the support constraint; the object is compact and all its electron density should lie within a certain three dimensional 3D volume, the support. The shrinkwrap method introduced by Marchesini *et al* [5, 19] uses a dynamic support constraint and has proved very successful in forward scattering phase retrieval experiments and more recently in the Bragg case [24]. The algorithm begins with the autocorrelation function as the first estimate of the illuminated object, several iterations of hybrid–input–output (HIO) and error reduction (ER) [10] are run and the support tailored to the current solution via a convolution operation with a $3 \times 3 \times 3$ voxel cube and smoothing with a Gaussian function. Further iterations of HIO and ER follow, the support is updated after each set of iterations. The algorithm converges when the support is found to be self consistent between algorithm iterations (less than 1% variance in shape). Although a valid approach, the shrinkwrap method outlined relies on the initial solution of pre-existing algorithms with a very loose support constraint, an enlarged copy of the autocorrelation function. In solution space a number of solutions are available with loose constraints, and are subsequently optimised by shrinking the support around them. The shrinkwrap method has optimized the solution based on the support constraint, it does not definitively identify the global minimum. It simply identifies a solution based on a set of loose constraints and optimizes it. From random starting points we would therefore expect and indeed observe a large variation in reconstructions but their supports are optimized. From this position we can apply the two approaches mentioned previously and find a more reliable average. The random starting point leads to multiple different solutions, in order to combine them the average phase needs to be set to zero [11], solutions need to be overlaid, ambiguous solutions such as twins (complex conjugate) identified and made equivalent and finally averaged together. The average solution must then be normalized to be used to seed further phasing iterations, seeding in this manner is similar to the guided HIO method demonstrated by Chen *et al* [6]. Here, structural features present in many solutions from multiple starting points are favoured as averaging weakens those which are less reproducible. These more prominent features are then used to drive the next generation of solutions until the algorithm converges.

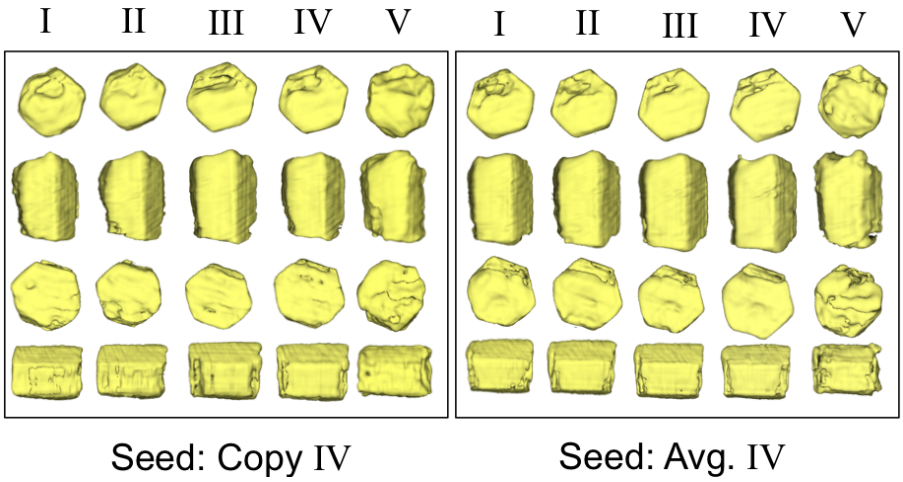

Figure 4. 3D renderings (top, front, bottom and rear views) of the reconstructed electron density amplitude isosurface after phasing using the copied and averaged phased solution from IV as a seed for the five measured diffraction patterns, I–V. Note all renderings are not on a commensurate scale but are in fact equivalent in size. Opposing facets in the hexagonal plane are separated by 1.1 μm and the hexagonal prism is 1.5 μm in length.

The first application of a phase constraint in DS was proposed by Miao *et al* [21]. All of the imaginary parts and 90% of the real parts were constrained to be positive, hence the allowed phase was confined between 0 and π. On this theme, Harder *et al* [12] employed a phase constrained HIO variant combined with ER to successfully reconstruct a compact complex object. More recently, Huang *et al* [14] explained its advantage in crystals with large phase structures akin to those observed in this study.

The following phasing operation was applied here. The datasets were individually phased using a copy of the support as the starting point to quickly home in on the correct phasing parameters. We applied 50 iterations of phase constrained-HIO, where the phase was constrained between $-\pi/2$ and $\pi/2$ keeping the real part positive, followed by 20 iterations of ER. Ten random starts were run for each diffraction pattern and the solutions shifted via cross correlation, twins identified and phase offsets applied. Once satisfied the constraints were correct, the random start solutions were averaged and normalized to the measured diffraction intensity. Two seed reconstructions for each diffraction pattern result; the averaged solution from random starts and a solution from the copy of the support. Cross correlation of the random solutions proceed, twins identified and a visual comparison completed to unify the seed solutions. A decision is now required with regards to which seed solution to use for the final phasing operation. If an obvious consistency between reconstructions was observed, the solutions were used as seed solutions. However, if no obvious similarity was observed, the three reconstructions with the lowest error metric were used as seed solutions for further phasing with the diffraction data to produce the final result[8].

The difference observed between the two seeded phasing procedures is shown in figure 4. From the diffraction patterns in figure 3 we know there was little change in the crystal before

[8] The phasing constraints were relaxed to the full 2π phase range.

the final annealing step (V), hence the first four reconstructions should be similar. It can be seen that as expected, the average seed produces a more consistent compact object for the first four reconstructions compared to that of the copy seed. The key features, of the order of 100 nm in size, are observed on the two ends of the crystal, whereas the copy seed solutions vary significantly on this scale between reconstructions.

5. Results: phase interpretation

To interpret the phase maps several predetermined phase modulations must be considered. In DS, the calculated phase corresponds to the displacement along the Q vector relative to an underlying equilibrium crystal lattice, $\phi = \vec{Q}.\vec{u}(r)$. In the positive Q vector direction a positive phase corresponds to an expansion, a negative phase corresponds to a compression. In the negative Q vector direction, a positive phase corresponds to a compression, a negative phase corresponds to an expansion. Fitting to the phase modulation will provide an insight into their physical origins. The FT operation requires the diffracted intensity to be centred in the array, if it is not linear gradients will result due to misalignment[9]. A quadratic phase structure could be caused by the shape of the x-ray beam, however this applies more readily to focused beam CXDI as the beam is of the order of the crystallite size, here the beam is over an order of magnitude larger than the probed sample, if modelled as a Gaussian over the 1–2 μm used the variation will be very small. Thus any modulation more complex than quadratic phase structure is likely a feature of the crystals structure.

Several defect structures are expected in ZnO crystals, such as oxygen and zinc vacancies. If these vacancies were to be uniformly distributed throughout the centre of the rod the atomic spacing in the crystal would be constant throughout the crystal thus the Bragg peak would simply shift. A contraction on the six hexagonal facets would not be expected as they are non-polar and atomically flat with an equal number of cations and anions in the surface plane. A contraction is predicted on the zinc face of the order 0.4 Å and limited to the very surface, thus, is likely below the resolution of the technique. However, if the sample were to be placed in vacuum an increase in oxygen vacancies at the surface would lead to a contraction near the facet relative to the rest of the crystal [28].

Phase maps corresponding to slices through the data presented in figure 4 are shown in figure 5. The phase structure is consistent with the reference measurement for the first three annealing steps and changes significantly after the final annealing step. The phase structures lie in the range $-\frac{3}{4}\pi < \phi < -\frac{1}{2}\pi$, the scale was set for clarity and extends to the full $\pm\pi$ phase range. Several regions of large phase gradients over short distances are present, the probable defect structures responsible for the asymmetry noted previously. The phase wraps observed at the top and base of the crystal were present for the three annealing steps and appear modified for the final iteration. In the interior of the crystal several modulations exist perpendicular to the Q vector direction.

For quantitative analyses of these structures a refraction correction is required. Refraction of the incident x-rays as they traverse the crystal is considerable for a micron sized sample and was applied according to Harder *et al* [13]. Scalar cut planes of phase modulation corrections shown in figure 6 are uniform along the c-axis direction. The optical path length of the scattered x-rays through the crystal remains approximately constant for each scatterer

[9] This feature is actually harnessed to correctly align the diffraction patterns to within a single pixel.

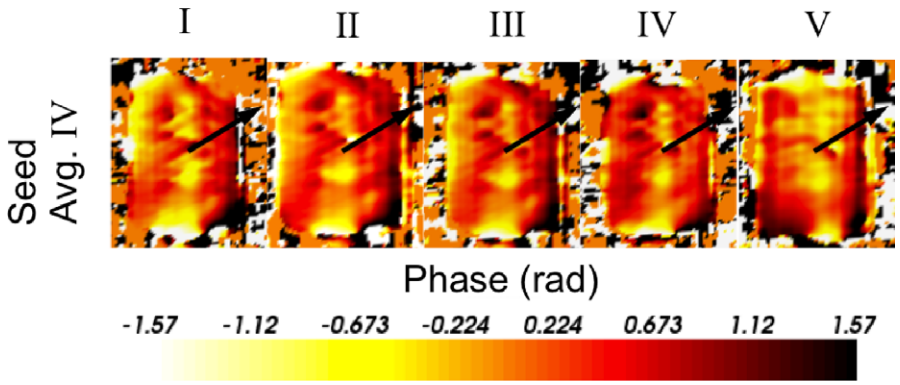

Figure 5. Phase cut planes, where the Q-vector (black arrow) lies in the plane, for the reconstruction of five consecutive diffraction datasets (I–V) using the average seed from IV as a starting point. The corresponding amplitude is demonstrated in figure 4.

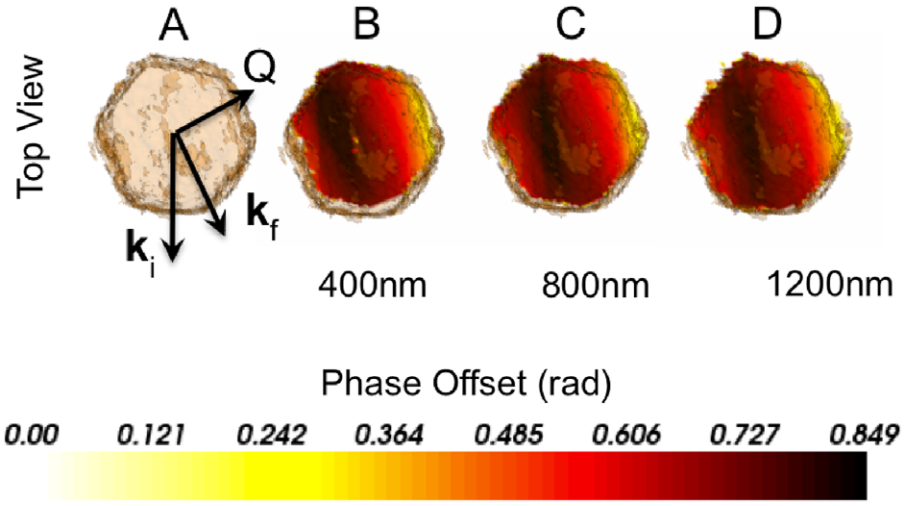

Figure 6. A top view of the refraction correction phase offset required for the reconstructed microrod, three phase maps extracted at different positions along and perpendicular to the *c*-axis direction. (A) A schematic of the geometry of the phase maps observed at (B) 400 nm, (C) 800 nm and (D) 1200 nm along the crystals *c*-axis.

in consecutive planes. The observed phase corrections themselves demonstrate an asymmetric phase modulation due to the optical path length of the scattered x-rays. The maximum phase modulation was observed left of the centre of the crystal along the negative Q-vector direction. The refraction correction was $\frac{1}{4}\pi$ at its peak and highlights an additional discrepancy when considering the origins of some of the phase modulations observed in reconstructed crystals. It does not detract from the evolution of the crystal morphology discussed previously which remains constant for every measurement.

The refraction phase correction was applied to IV for closer inspection of the observed defect structure, see figure 7. The slices taken at different positions along the crystal *c*-axis

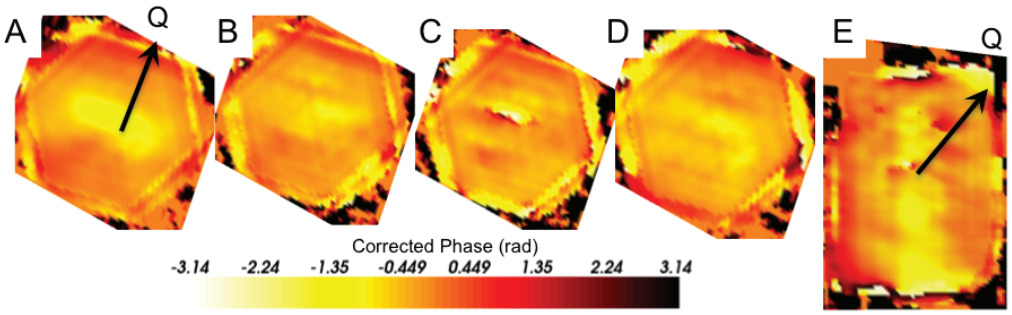

Figure 7. Four scalar cut planes in the hexagonal plane through the refraction corrected phase at (A) 300 nm, (B) 600 nm, (C) 900 nm and (D) 1200 nm along the length of the rod, and (E) a single cut plane where the c-axis and Q vector lie in the plane.

demonstrate several interesting features. Towards the surfaces the phase modulates between $\pm\frac{\pi}{2}$ and can be seen to be modulated perpendicular to each facet. At the very edges at the order of the resolution of the data the phase modulates rapidly and is attributed to the rapid fall away in electron density. Here, the amplitude is close to zero, thus the phase becomes meaningless. This is further compounded by the refraction correction being applied to only those data points above the electron density threshold and leads to a distinct step in the phase. The phase gradient across the crystal is nonlinear, positive along $+Q$ and negative along $-Q$ suggesting an expansion towards the surfaces. The third slice demonstrates the most significant defect structure, the phase wraps along the Q vector direction over 100nm and 300nm in width. Three phase structures are present in the crystal, two of which are accompanied by regions of low electron density and the third simply exhibits a large phase modulation which joins with one of the other defect structures. The low density region is probably due to a complex defect structure which cannot, at present [23], be recovered using the current phase retrieval method and not due to a void in the crystal. In the final slice through the c-axis of figure 7, the phase of the central defect structure appears to be modulated perpendicular to the Q vector direction, this could be understood as the presence of a dislocation loop structure whereby a shift of the crystal relative to the underlying crystal lattice would be observed above and below the loop in opposing directions. For a single dislocation loop we would expect to observe the perpendicular phase modulation along the length of the defect, in this case the phase modulates non-uniformly across the defect suggesting a more complex defect than a simple dislocation loop. Upon further annealing the electron density local to the phase modulation drops suggesting the crystal has changed in this region, the two other low density regions also increase in size. The degradation of the crystal's exterior was large compared to the other observed defect structures. Although quantitative displacements cannot be calculated in this region we can qualitatively assign the loss of recovered electron density to either the formation of secondary phases or the presence of complex defect structures. The distortion present on the base of the crystal was determined, via energy dispersive x-ray spectroscopy, to correspond to zinc diffusion into the substrate during sample fabrication.

The nickel experiments demonstrated a general trend towards crystal degradation and was expected from the diffraction data, the reconstructions however were inconsistent. The amplitude distribution was very asymmetric and not expected for single crystal rods. The source of this feature was deduced to be the longitudinal coherence length [17]. The experimental

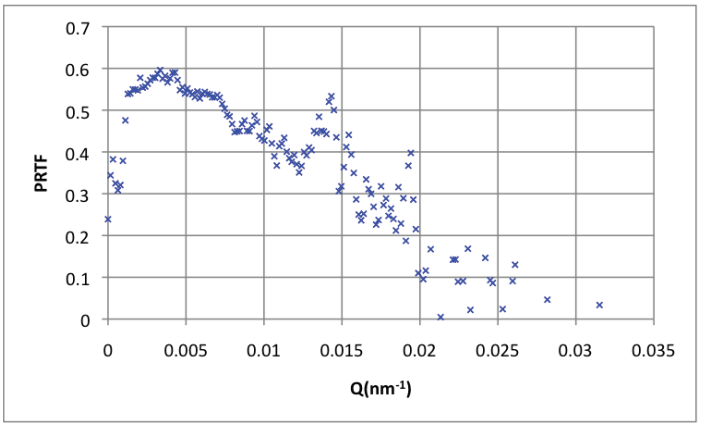

Figure 8. PRTF of a reconstructed solution generated from 10 random starting points using the shrinkwrap algorithm for support optimization.

parameters were harder to pin down. A large change was observed after the final annealing step and the phasing algorithms struggled to find a uniform DS amplitude distribution. Agreement was observed between the phase modulation before the onset of the reaction after which the crystal had changed sufficiently to prevent the observation of the evolution of the phase modulations present. The low solubility of Ni in ZnO suggests changes of this nature are unlikely to be a result of Ni integration into the ZnO lattice but rather NiO cluster formation.

When we discuss image resolution we separate the phases and the amplitudes. A single wrap in the phase across a crystal corresponds to a shift from the equilibrium lattice by a single lattice parameter along the Q-vector direction. The resolution of the phase is difficult to quantify and is defined by the asymmetry around a Bragg reflection[10]. Typically phase changes of the order 0.15 rad are resolvable corresponding to 1/40th of a ZnO lattice parameter. The phase modulation describes the relative shift of a portion of crystal the size of which is defined by the resolution of the amplitude. The resolution of the amplitude can be estimated by the phase retrieval transfer function (PRTF) [5, 29], from equivalent solutions the reproducibility of the reconstructed phases at every spatial frequency can be tested. A perfect average reconstruction would produce a step function, with a cutoff at the resolution limit.

Figure 8 demonstrates the PRTF generated from 10 random starting points. The threshold intensity was set to approximately 10 photons (1600 ADUs). At low Q, corresponding to large length scales in DS, the PRTF appears unstable. We would predict this to be constant and closer to unity, and expect this is due to a lack of statistics. The PRTF averages all pixels in concentric shells of width δQ as a function of Q away from the Bragg peak. Thus, the first datapoint considers only 7 voxels compared to up to 45 000 voxels at higher frequencies. The resolution is deduced at the point when the PRTF drops to $1/e$ [29]. In this case, at 0.015 nm^{-1}. Thus a resolution of 67 nm (33 nm half period) was expected. This is commensurate with the fringe counting method. Given significant statistics were observed out to approximately the 15th fringe (f_n) of the diffraction pattern and the crystal is 1μm in size the resolution is simply estimated by $\frac{\mathrm{size}}{f_n}$.

[10] However, if symmetric phase structures are present, i.e. an inward displacement on one side of the crystal and an outward displacement on the other, the signal will remain symmetric.

6. Summary

A ZnO microcrystal was covered in an Fe layer and observed using CXDI *in situ* after several annealing steps. The onset of a solid state reaction was observed. The diffraction patterns collected were successfully analysed using a phase retrieval method which utilised both averaging and seeding to obtain agreement between subsequent experimental iterations. The electron density was recovered with 33 nm half period resolution with sub-Angstrom sensitivity to displacements in the lattice. Several prominent phase structures decorate the interior of the crystal. One demonstrated large phase modulation and was attributed to a complex defect structure. The other large phase modulations present had characteristic voids of electron density arising from large displacements yet to be resolved with current phase retrieval methods without a well known *a priori* support constraint [22]. Upon annealing, the internal defect structures increased in size. The degradation of the exterior of the crystal was too great to observe an evolution of the phase structure. However, the sensitivity of CXDI suggests the degraded regions are either secondary phases or riddled with complex defect structures. Evaporation of metal onto the surface is thus not a suitable method for doping ZnO microrods. The distortion present on the base of the crystal was attributed to zinc diffusion into the substrate during sample fabrication.

Acknowledgments

The CXDI instrument at Advanced Photon Source beamline 34ID-C was built with the US National Science Foundation grant DMR-9724294. This document was prepared by University College London as a result of the use of facilities (Advanced Photon Source and Electron Microscopy Center) of the US Department of Energy (DOE), which are managed by UChicago Argonne, LLC, acting under contract no. DE-AC02-06CH11357. Neither UChicago Argonne, LLC, DOE, the US Government, nor any person acting on their behalf: (a) make any warranty or representation, express or implied, with respect to the information contained in this document; or (b) assume any liabilities with respect to the use of, or damages resulting from the use of any information contained in the document.

References

[1] Baek S, Song J and Lim S 2007 Improvement of the optical properties of ZnO nanorods by Fe doping *J. Phys.: Condens. Matter* **399** 101–4

[2] Bates C H, White W B and Roy R 1966 The solubility of transition metal oxides in zinc oxide and the reflectance spectra of Mn^{2+} and Fe^{2+} in tetrahedral fields *J. Inorg. Nucl. Chem.* **28** 397–405

[3] Baxter J B and Schmuttenmaer C A 2006 Conductivity of ZnO nanowires, nanoparticles and thin films using time-resolved terahertz spectroscopy *J. Phys. Chem.* B **110** 25229–39

[4] Bruck Y M and Sodin L G 1979 On the ambiguity of the image reconstruction problem *Opt. Commun.* **30** 304–8

[5] Chapman H N, Barty A, Marchesini S, Noy A, Hau-Riege S P, Cui C, Howells M R, Rosen R, He H and Spence J C H 2006 High-resolution *ab-initio* three-dimensional x-ray diffraction microscopy *J. Opt. Soc. Am.* A **23** 1179–200

[6] Chen C-C, Miao J, Wang C and Lee T 2007 Three-dimensional image reconstruction of radiation-sensitive samples with x-ray diffraction microscopy *Phys. Rev.* B **76** 064113

[7] Davies R, Abernathy C R, Pearton S J, Norton D P, Ivill M P and Ren F 2009 Review of recent advances in transition and lanthanide metal-doped GaN and ZnO *Chem. Eng. Commun.* **196** 1030–53

[8] Dietl T, Matsukura F and Ohno H 2002 Ferromagnetism of magnetic semiconductors: Zhang–Rice limit *Phys. Rev.* B **66** 033203
[9] Elser V 2003 Solution of the crystallographic phase problem by iterated projections *Acta Crystallogr.* A **59** 201–9
[10] Fienup J R 1978 Reconstruction of an object from the modulus of its Fourier transform *Opt. Lett.* **3** 27–9
[11] Fienup J R 1997 Invariant error metrics for image reconstruction *Appl. Opt.* **36** 8352–7
[12] Harder R, Liang M, Sun Y, Xia Y and Robinson I K 2010 Imaging of complex density in silver nanocubes by coherent x-ray diffraction *New J. Phys.* **12** 035019
[13] Harder R, Pfeifer M, Williams G, Vartaniants I and Robinson I 2007 Orientation variation of surface strain *Phys. Rev.* B **76** 115425
[14] Huang X, Harder R, Xiong G, Shi X and Robinson I 2011 Propagation uniqueness in three-dimensional coherent diffractive imaging *Phys. Rev.* B **83** 224109
[15] Jin Z, Fukumura T, Kawasaki M, Ando K, Saito H, Sekiguchi T, Yoo Y Z, Murakami M, Matsumoto Y and Hasegawa T 2001 High throughput fabrication of transition-metal-doped epitaxial ZnO thin films: a series of oxide-diluted magnetic semiconductors and their properties *Appl. Phys. Lett.* **78** 3824
[16] Leake S J 2010 Coherent x-ray diffraction imaging of zinc oxide crystals *PhD Thesis* University College London, pp 1–277
[17] Leake S J, Newton M C, Harder R and Robinson I K 2009 Longitudinal coherence function in x-ray imaging of crystals *Opt. Express* **17** 15853–9
[18] Mandal S K, Das A K, Nath T K and Karmakar D 2006 Temperature dependence of solubility limits of transition metals (Co, Mn, Fe and Ni) in ZnO nanoparticles *Appl. Phys. Lett.* **89** 144105
[19] Marchesini S, He H, Chapman H, Hau-Riege S, Noy A, Howells M, Weierstall U and Spence J 2003 X-ray image reconstruction from a diffraction pattern alone *Phys. Rev.* B **68** 140101
[20] Miao J, Charalambous P, Kirz J and Sayre D 1999 Extending the methodology of x-ray crystallography to allow imaging of micrometre-sized non-crystalline specimens *Nature* **400** 342–4
[21] Miao J, Sayre D and Chapman H N 1998 Phase retrieval from the magnitude of the Fourier transforms of nonperiodic objects *J. Opt. Soc. Am.* A **15** 1662–9
[22] Minkevich A A, Gailhanou M, Micha J S, Charlet B, Chamard V and Thomas O 2007 Selective coherent x-ray diffractive imaging of displacement fields in (GaMn)As/GaAs periodic wires *Phys. Rev.* B **76** 104106
[23] Newton M, Harder R, Huang X and Xiong G 2010 Phase retrieval of diffraction from highly strained crystals *Phys. Rev.* B **82** 165436
[24] Newton M C, Leake S J, Harder R and Robinson I K 2009 Three-dimensional imaging of strain in a single ZnO nanorod *Nature Mater.* **9** 120–4
[25] Pfeifer M A, Williams G J, Vartanyants I A, Harder R and Robinson I K 2006 Three-dimensional mapping of a deformation field inside a nanocrystal *Nature* **442** 63–6
[26] Robinson I K, Vartanyants I A, Williams G J, Pfeifer M A and Pitney J A 2001 Reconstruction of the shapes of gold nanocrystals using coherent x-ray diffraction *Phys. Rev. Lett.* **87** 195505
[27] Sayre D 1952 Some implications of a theorem due to Shannon *Acta Crystallogr.* **5** 843
[28] Schmidt O, Kiesel P, Van De Walle C G, Johnson N M, Nause J and Döhler G H 2005 Effects of an electrically conducting layer at the zinc oxide surface *J. Appl. Phys.* **44** 7271–4
[29] Shapiro D, Thibault P, Beetz T, Elser V, Howells M, Jacobsen C, Kirz J, Lima E, Miao H and Neiman A M 2005 Biological imaging by soft x-ray diffraction microscopy *Proc. Natl Acad. Sci. USA* **102** 15343
[30] Ueda K, Tabata H and Kawai T 2001 Magnetic and electric properties of transition-metal-doped ZnO films *Appl. Phys. Lett.* **79** 988–90
[31] Wang R, Sleight A W and Subramanian M A 1996 An unusual iron site in iron-doped zinc oxide *J. Solid State Chem.* **125** 224–7
[32] Wei X X, Song C, Geng K W, Zeng F, He B and Pan F 2006 Local Fe structure and ferromagnetism in Fe-doped ZnO films *J. Phys.: Condens. Matter* **18** 7471
[33] Williams G J 2006 Microscopy of gold microcrystals by coherent x-ray diffractive imaging *PhD Thesis* University of Illinois, pp 1–226